Science
AAAS

Supplementary Materials for

Ultrafast mode-locked laser in nanophotonic lithium niobate

Qiushi Guo *et al*.

Corresponding authors: Qiushi Guo, qguo@gc.cuny.edu; Alireza Marandi, marandi@caltech.edu

Science **382**, 708 (2023)
DOI: 10.1126/science.adj5438

The PDF file includes:

Materials and Methods

Device fabrication: We fabricated the integrated waveguides, phase modulators, and broadband loop mirrors on a 700-nm-thick X-cut MgO-doped LN thin-film on 4.7-μm-thick SiO_2 on top of a silicon substrate (NANOLN). We first patterned the waveguides using e-beam lithography by employing Hydrogen Silsesquioxane (HSQ) as the e-beam resist. The designed top width of the LN waveguide is 800 nm. The LN layer was etched by 350 nm using Ar^+ plasma. This etching process yields a waveguide sidewall angle of $\sim 60^\circ$. Next, we deposited an 800 nm SiO_2 cladding layer using plasma-enhanced chemical vapor deposition (PECVD). Another e-beam lithography step was used to pattern the RF metal electrodes on top of the cladding layer, in which PMMA was used as the e-beam resist. Then, we deposited Cr/Au (10 nm/300 nm) using e-beam evaporation. Metal electrodes are formed after metal lift-off in acetone. To ensure a 50 Ω impedance around 10 GHz, the width of the RF signal and ground electrode are designed to be 8 μm and 28 μm, respectively. The gap size between the signal and ground electrodes is 4 μm, and the thickness of the electrodes is 300 nm. Finally, the waveguide facets were mechanically polished to enable good light coupling efficiencies.

Optical measurements: For butt-coupling the SAF gain chip (Photodigm Inc.) and the TFLN chip together, the SAF gain chip was placed on a 6-axis nano-positioning stage (Thorlabs) and the TFLN chip was clamped on a fixed sample stage. The two chips could be visually aligned by using a microscope from above. After visual alignment, the alignment was further optimized by maximizing the output power measured by a power meter, which is related to the intra-cavity optical power of the laser. The output power of the MLLs is probed by a single-mode lensed fiber (OZ optics Ltd.) connected to an optical power meter (Thorlabs). The RF drive is provided by an RF signal generator (Rohde & Schwarz SMA100B) and is subsequently amplified by a high-power RF amplifier (Mini-Circuits ZVE-3W-183+). The input RF power is calibrated by an RF power meter (Ladybug). For the results in Fig. 3-5, the laser output spectra were collected by an optical spectrum analyzer (OSA) covering 600-1700 nm (Yokogawa AQ6370B) with a 0.01 nm resolution bandwidth. The heterodyne beat notes between two neighboring laser emission lines and a narrow-linewidth ($\sim$10 kHz) reference CW tunable laser (CTL, Toptica) were collected by a fast photodetector (Thorlabs DXM30AF). The RF spectra of the heterodyne beat note were collected by an electronic spectrum analyzer (Rohde & Schwarz FSW) with a 100 Hz resolution bandwidth. In order to get intensity autocorrelation with a good signal-to-noise ratio, we pre-amplified the laser output power by a Ytterbium-doped fiber amplifier (YDFA, Pritel Inc.). We also used a pulse shaper to compensate for the group velocity dispersion (GVD) imposed by the phase modulator, YDFA (Pritel), and the single-mode fiber.

Numerical simulations: The optical and RF field distributions shown in Fig. 2a in the main text were simulated by COMSOL Multiphysics. We also used commercial software (Lumeriacl MODE, Ansys Inc.) to solve for the waveguide modes in order to design the waveguide taper and obtain the dispersion characteristics of the waveguide. In the simulation, the anisotropic index of the LN was modeled by the Sellmeier equations[40].

Supplementary Text

I. DESIGN OF THE BROADBAND LOOP MIRROR

Achieving uniform mirror reflection that covers the entire laser gain spectrum is crucial for short pulse generation in integrated mode-locked lasers. In integrated photonic platforms, integrated loop mirrors can offer a broad reflection bandwidth. However, the reflectance of a loop mirror is determined by the coupling ratio of a directional coupler, which is typically wavelength-dependent. To mitigate this wavelength dependence and achieve broader reflection bandwidth in the loop mirror, we adopted a curved directional coupler (CDC) design as elaborated in Ref.[41, 42]. As shown in Fig. S1, our integrated loop mirror has a CDC region with a bending radius of 600 μm. The total length of the curved coupling region is 50 μm.

Figure S2 compares the performance of loop mirrors with different directional coupler configurations. The operating wavelength range of interest is from 1020 to 1100 nm. As shown in Fig. S2a, with a straight direction coupler, the reflectance of the loop mirror strongly depends on the operating wavelength. With a CDC of bending radius of 600 nm (Fig. S2c), the loop mirror almost exhibits no wavelength dependence within the wavelength range of interest. With a coupling length of ~45 μm, near 100% reflection is achieved across the desired wavelengths.

In addition, as shown in Fig. S3, our designed loop mirror has a negligible reflection at 532 nm, which is the second harmonic of the 1064 nm laser. This particular attribute plays a crucial role in preventing resonance of the generated 532 nm light within the laser cavity. Such resonance has the potential to induce photorefractive damage to the LN waveguide and disrupt the optimal functioning of the gain medium.

II. COUPLING BETWEEN THE GAIN CHIP AND THE THIN-FILM LITHIUM NIOBATE CHIP

The TFLN chip is butt-coupled to an edge-emitting semiconductor optical amplifier (SOA). To maximize the power coupling, it is pertinent to ensure the mode overlap between the SOA output and the TFLN chip waveguide facet is maximized. Implementing an adiabatic taper is one method to achieve this. This style of taper improves the mode overlap in one dimension, which can significantly increase the total mode overlap. Alas, the mode mismatch in the remaining transverse dimension can not be accommodated for by such a simple adiabatic taper. For this reason, it is important to carefully select a source such that the mode mismatch in this constrained transverse dimension is maximized to begin with. To select a proper source, an estimate of the mode size at the output of the source is needed. With this, it is possible to determine if the source is a good choice for the designed waveguide mode of the photonic chip. A commonly listed specification for commercial sources is the far-field divergence angle of the full-width half-maximum intensity profile. The following discusses how to estimate the output mode size of a source given this specification. As the gain chips considered for this design all exhibited a single spatial mode, single-mode Gaussian profiles are assumed in this analysis. This estimation is then used to inform the choice of gain chip implemented in the design. Next, mode overlap simulations are performed using Lumerical MODE to optimize the taper width such that the mode overlap in the unconstrained dimension is maximized. Finally, the length of the adiabatic taper is designed to ensure high transmission. This straightforward process enables efficient coupling between the gain chip and the photonic circuit.

A. Single mode Gaussian beam divergence

For Gaussian beam diffraction, the beam radius at the 1/e point of the electric field is given by,

$$w^2(z) = \omega_0^2 \left[1 + \left(\frac{\lambda z}{\pi w_0^2 n}\right)^2\right] \tag{1}$$

where n is the refractive index of the medium the beam propagates through, λ is the free-space wavelength, z is the axial distance from the beam's waist, w_0 is the waist radius [43]. In the far field ($z \gg \frac{\pi w_0^2 n}{\lambda}$), we can simplify Eq. 1 to

$$w(z) \approx \frac{\lambda z}{\pi n w_0} \tag{2}$$

Additionally, the far-field diffraction half-apex angle at the 1/e point of the electric field, θ_e, can be defined as,

$$\tan(\theta_e) = \frac{w(z)}{z} \tag{3}$$

Then, we can express the waist (radius) of the 1/e point of the electric field as

$$w_0 \approx \frac{\lambda}{\pi n \tan(\theta_e)} \tag{4}$$

B. Electric field and intensity relationship

Specification sheets for commercially available semiconductor gain chips typically list the divergence angle of the FWHM far-field intensity profile. However, up until this point, the equations listed are based on the 1/e point of the electric field. So there is a need to connect the equations above to the specification sheets of these gain chips. At a specified propagation distance, the Gaussian profiles of the electric field and intensity are related by,

$$E(r) = e^{-r^2/2\sigma^2} \tag{5}$$

$$I(r) \propto |E(r)|^2 = e^{-r^2/\sigma^2} \tag{6}$$

where the magnitudes of the profiles have been neglected. To determine the relationship between the half-apex angle of the electric field at the 1/e point and the half-apex angle of the FWHM intensity profile, a relationship between the waist radii at each of these points must be established. Since the radii at which each of these profiles achieves a specific value is different, r in equations 5 and 6 must be replaced with r_i or r_e respectively. The FWHM of the intensity profile becomes,

$$\frac{1}{2} = e^{-r_i^2/\sigma^2} \tag{7}$$

$$r_i^2 = -\ln(0.5)\sigma^2 \tag{8}$$

The 1/e point of the electric field profile becomes,

$$\frac{1}{e} = e^{-r_e^2/2\sigma^2} \tag{9}$$

$$r_e^2 = 2\sigma^2 \tag{10}$$

The ratio of the FWHM intensity and 1/e electric field radii is

$$\frac{r_i}{r_e} = \sqrt{-\ln(0.5)/2} \tag{11}$$

Now, both of these radii will occur at some shared propagation distance z away from the beam waist, given as

$$z = \frac{r}{\tan(\theta)} \tag{12}$$

So we can find the relationship between the radii and their half-apex angles as,

$$\frac{r_i}{\tan(\theta_i)} = \frac{r_e}{\tan(\theta_e)} \tag{13}$$

$$\frac{1}{\tan(\theta_e)} = \frac{r_i}{r_e}\frac{1}{\tan(\theta_i)} \tag{14}$$

where θ_e is the half-apex angle of the 1/e point of the electric field and θ_i is the half-apex angle of the FWHM point of the intensity. Gathering equations 4, 11 and 14, the waist of the electric field can be expressed as

$$\omega_0 \approx \frac{\lambda}{\pi n \tan(\theta_e)} = \frac{\lambda}{\pi n}\frac{r_i}{r_e}\frac{1}{\tan(\theta_i)} = \frac{\lambda}{\pi n}\frac{\sqrt{-\ln(0.5)/2}}{\tan(\theta_i)}$$

So finally, taking $n = 1$, we can convert directly from the spec sheet parameter of divergence angle at FWHM of the intensity to the waist (radius) of the electric field as

$$\omega_0 \approx \frac{\lambda}{\pi \tan(\theta_i)}\sqrt{\frac{-\ln(0.5)}{2}} \tag{15}$$

With this estimation, we can now quickly evaluate which gain chip options have a high mode overlap in the constrained dimension with our chosen waveguide structure.

C. Chip coupling loss calculation

The single-angle facet (SAF) gain chip (Photodigm) used in the experiment is listed as having a full-apex divergence angle at the full-width half-maximum (FWHM) point of the electric field as 26° in the fast-axis (vertical) and 6° in the slow-axis (horizontal). This gain chip emits around 1064 nm. Using x to denote the horizontal axis and y to denote the vertical axis, we can express the half-apex angles as $\theta_{i,x} = 3°$ and $\theta_{i,y} = 13°$. Using equation 15, we find the mode waist of the electric field at the 1/e point to be

$$\omega_{0,x} \approx \frac{\lambda}{\pi \tan(\theta_{i,x})}\sqrt{\frac{-\ln(0.5)}{2}} = \frac{1064}{\pi \tan(3°)}\sqrt{\frac{-\ln(0.5)}{2}} = 3.804\,\mu\text{m} \tag{16}$$

for the x-axis and

$$\omega_{0,y} \approx \frac{\lambda}{\pi \tan(\theta_{i,y})}\sqrt{\frac{-\ln(0.5)}{2}} = \frac{1064}{\pi \tan(13°)}\sqrt{\frac{-\ln(0.5)}{2}} = 864\,\text{nm} \tag{17}$$

for the y-axis. The constrained (vertical) dimension for this gain chip is found to have a high mode overlap with our chosen TFLN waveguide structure, making it a good choice for our application. A TFLN adiabatic taper can then be implemented to match the remaining horizontal dimension. To do this, mode overlap simulations are performed using Lumerical's finite-difference eigenmode (FDE) solver. The power coupling can then be calculated for various waveguide taper widths. To optimize the taper width, the power coupling is calculated as the taper width is swept, as shown in Fig. S4. Assuming there is no vertical misalignment, horizontal misalignment, and gap between the gain chip and TFLN chip, a waveguide taper top width of 10.3 μm yields a coupling loss of 1.73 dB.

However, in practical experiments, the coupling loss induced by mode size mismatch may exceed 1.73 dB due to various factors, including vertical misalignment, horizontal misalignment, and the gap between the SAF gain chip and the TFLN chip. As can be seen in Fig. S5a, when the SOA is misaligned vertically from the adiabatic taper, the coupling loss increases significantly. However, as shown in Fig. S5b, the coupling loss is less sensitive to horizontal misalignment. This is due to the strong vertical confinement of fundamental TE modes within both the SAF gain chip and the TFLN chip, whereas their horizontal confinement is comparatively weaker. Moreover, Fig. S5c shows that when there is 1 μm gap between the two chips, the coupling loss increases from 1.73 dB to 2 dB. In our experiments, we carefully reduced the gap size below 1 μm, as can be seen from Fig. 2g in the main text. However, due to the chip facet quality and imperfection of vertical and horizontal alignment in our experiment, we expect that the coupling loss due to mode size mismatch is $\sim$ 2.5 to 3 dB.

The dominant coupling loss mechanism is the mismatch in light field confinement between the SAF gain chip and the TFLN chip in the vertical direction, as the TFLN layer is thinner than the active layer in the SAF gain chip. To further increase the coupling efficiency between the two platforms, we can employ an inverted taper edge coupler embedded in a polymer waveguide on TFLN [30]. This design can further expand the light field within the TFLN waveguide along the vertical axis, which enables a better match of the mode size in the SAF gain chip. It has been shown in the silicon nitride platform that the technique can result in a 90% mode overlap between both chips, yielding a coupling loss of $\sim$1 dB [31]. Moreover, this approach can also significantly reduce reflection at the air/LN interface.

D. Design of the linear taper

All that remains is determining a proper taper length to ensure high transmission. Burns et al. provided a design rule for tapered waveguides that describes the maximum allowable taper angle needed for adiabatic mode conversion [44]. For a waveguide of width W, the maximum half apex taper angle is approximated by

$$\theta_{\max} \approx \frac{\lambda_0}{2nW} \tag{18}$$

where λ_0 is the freespace wavelength, and n is the bulk index of the medium. As the waveguide width expands, the maximum allowable angle flattens out leading to a parabolic taper profile. However, in the linear case, the taper angle is chosen to satisfy this condition at both the input and output taper widths. This condition is then set by the widest part of the taper which results in the most stringent maximum angle condition. In our case, the taper has a maximum width of 10.3 μm, which results in a maximum half-apex angle of 1.32°. Tapering from 10.3 μm down to the waveguide width of 800 nm at a maximum half-apex angle of 1.32° requires a minimum taper length of $\sim$200 μm. For this design, the taper was chosen to be 250 μm to ensure adiabatic mode conversion and high transmission.

III. CALCULATION OF CAVITY GROUP DELAY DISPERSION

As illustrated by Fig. 1a in the main text, the laser cavity is composed of five sections: 1) a 10.3 μm-wide waveguide input region with a length of $\sim L_{\mathrm{w}} = 1$ mm, 2) a linear waveguide taper section with a length of $L_{\mathrm{t}} = 0.25$ mm, 3) a straight waveguide section with a length of $L_{\mathrm{s}} = 1.5$ mm, 4) a directional coupler section with a length of 50 μm, and 5) a loop mirror section with a length of $L_{\mathrm{l}} = 440$ μm. The total group delay dispersion (GDD) of the cavity can be estimated by the sum of the GDD of each section. We employed ANSYS Lumerical MODE to simulate the group velocity dispersion (GVD) of the fundamental TE mode in each section by considering the waveguide cross-sectional geometry. As shown in Fig. S6, at the laser center wavelength of 1064.8 nm, the straight waveguide yields a normal GVD of 131.1 fs^2/mm, the loop mirror section with 70 μm bending radius has a normal GVD of 135.7 fs^2/mm. Moreover, the widest region (10.3 μm in top width) of the linear waveguide taper has a normal GVD of 108.5 fs^2/mm. Assuming the GVD in the waveguide taper region varies linearly with the waveguide top width, the averaged GVD in the waveguide taper region ($\mathrm{GVD_t}$) can be estimated as (131.1+108.5)/2=119.8 fs^2/mm. Since the directional coupler section is very short compared to other sections, its contribution to the total GDD is negligible. The total GDD per cavity round trip is estimated by $\mathrm{GDD_{roundtrip}} = 2 \times (\mathrm{GVD_w} \cdot L_{\mathrm{w}} + \mathrm{GVD_t} \cdot L_{\mathrm{t}} + \mathrm{GVD_s} \cdot L_{\mathrm{s}}) + \mathrm{GVD_l} \cdot L_{\mathrm{l}} = 861$ fs.

IV. ANALYSIS OF LASER OUTPUT PULSE WIDTH

A. Pulse width limit estimation using Haus's master equation

In this section, we estimate the fundamental pulse width limit of our actively MLL by considering the simplest case, which neglects the nonlinear optical effects in the laser cavity, and the complex carrier dynamics in the gain medium. In this case, the output pulse width can be analytically solved from Haus's master equation (HME). The HME considering the total pulse shaping due to gain, loss, cavity dispersion, and intra-cavity phase modulation can be written as [33]:

$$T_{\mathrm{R}}\frac{\partial A(T,t)}{\partial T} = [\ g(T) - l + (D_{\mathrm{g}} + iD)\frac{\partial^2}{\partial t} \mp iM\cos(\omega_{\mathrm{m}}t)]A(T,t) \tag{19}$$

where T_{R} is the round-trip time of the laser cavity, $g(T)$ is the time-dependent gain, D_{g} is the gain dispersion, D is half of the cavity round-trip GDD, $M = \pi V_{\mathrm{pp}}/V_{\pi}$ is the modulation index of the phase modulator, and $\omega_{\mathrm{m}} = 2\pi f_{\mathrm{m}}$ is the angular frequency of the RF signal applied to the phase modulator. The two signs on the phase modulation term indicate solutions may exist at each extremum of phase variation. The time scale t describes the detailed time dependence of the pulse envelope $A(T,t)$, and the longer time scale T describes the temporal changes over the course of several resonator roundtrip times T_{R} (i.e. $t \ll T_{\mathrm{R}}$ and $T \gg T_{\mathrm{R}}$). We then simplify Eq. 19 by assuming a fixed saturated gain value in the steady state ($g(T) = g$). We expect the pulses will have a width much shorter than the round-trip time T_{R}. They will be located in the minimum or maximum of the intra-cavity phase modulation, where a Taylor expansion to second order of the cosine function gives $\cos(\omega_{\mathrm{m}}t) \approx 1 - (\omega_{\mathrm{m}}t)^2/2$. We thus obtain

$$T_{\mathrm{R}}\frac{\partial A(T,t)}{\partial T} = [g - l + (D_{\mathrm{g}} + iD)\frac{\partial^2}{\partial t^2} \mp iM(1 - \omega_{\mathrm{m}}^2 t^2/2)]A(T,t) \tag{20}$$

where $D_{\mathrm{g}} = g/(\pi\Delta f_{\mathrm{g}})^2$ is the gain dispersion and Δf_{g} is the 3 dB gain bandwidth. The solution ansatz of Eq. 20, which satisfies the steady-state condition $T_{\mathrm{R}}\partial A(T,t)/\partial T = 0$, is a chirped Gaussian pulse in the form of:

$$A(t) = A_0 \exp\left[-\frac{1}{2}\frac{t^2}{\tau^2}(1 - i\beta)\right] \tag{21}$$

where β is the chirp parameter. Substituting Eq. 21 to Eq. 20, and solving for the chirp parameter produces

$$\beta_{\pm} = \pm\frac{D_{\mathrm{g}}}{D^2 + D_{\mathrm{g}}^2}\frac{M\omega_{\mathrm{m}}^2\tau^4}{4} = \frac{D \pm \sqrt{D^2 + D_{\mathrm{g}}^2}}{D_{\mathrm{g}}}. \tag{22}$$

It can be seen from Eq. 22 that two distinct solutions arise from the HME with GDD. In one case, the phase modulator compensates for the chirp imposed by the cavity GDD while in the other case the phase modulator adds to the GDD chirp. The resulting pulses have FWHM Gaussian pulse durations of

$$\tau_{\mathrm{p}} = \sqrt{8\ln 2}\left[\frac{(D^2 + D_{\mathrm{g}}^2)(\sqrt{D^2 + D_{\mathrm{g}}^2} \pm D)}{D_{\mathrm{g}}^2 M\omega_{\mathrm{m}}^2}\right]^{1/4}. \tag{23}$$

In section IV, we calculate a round-trip GDD of 861 fs^2 for the TFLN chip. We also estimate the GDD of the SAF gain chip by using a bulk GVD value of 3725.6 fs^2/mm for GaAs at 1065 nm. For our gain chip length of 1.5 mm, the round-trip length is 3 mm, so the round-trip GDD imposed by the gain chip is 11176.8 fs^2. Thus the total cavity GDD is 12037.8 fs^2. Given the calculated V_{π} of our phase modulator of 10.67 V, with 280 mW RF driving power ($V_{\mathrm{pp}} = 3.74$ V), the modulation index (M) is estimated to be 1.1. In steady-state, the saturated gain g must equal the round-trip loss l. Since g is the round-trip exponential gain coefficient for the electric field, we may calculate its steady-state value given the power loss per round-trip, denoted T, as $g \approx l = -\ln\left(\sqrt{1-T}\right) = -\ln(1-T)/2$, where the factor of two comes from taking the square of the electric field to translate from power loss to field loss. Considering the round-trip power loss of 90% due to chip-to-chip coupling loss, the output coupling loss, and the waveguide propagation loss, the saturated gain g is found to be $-\ln(1-0.9)/2 = 1.15$. Moreover, the 3 dB gain bandwidth of our gain chip is ~ 4 THz. At an RF driving frequency of $f_{\mathrm{m}} = 10.17$ GHz, these parameters result in Gaussian pulses with characteristics listed in Table S1. These results suggest that cavity dispersion can compensate for the chirp of the phase modulator to create near transform-limited pulses.

B. Pulse width limit estimation using split-step Fourier transform simulation

Next, we investigate the discrepancy of predicted pulse widths with those that were observed in the experiment. We compare the analytic results to a split-step Fourier transform simulation of the HME with GDD. This approach does not make use of the approximations that led to the above analytic equations. However, for the same parameters, we find good agreement with the analytic expressions. Figure S7a and S7d show the chirped and transform-limited pulses for the β_- and β_+ solutions, respectively. In addition to finding the steady-state solution for the cited experimental parameters, we also sweep loss and gain bandwidth to show their effect on pulse width and chirp. These sweeps demonstrate how uncertainty in these parameters leads to significant deviation in the pulse width and chirp predicted by the HME in some cases by greater than a factor of two. Pulses on the order of 4-5 ps, as observed experimentally, can easily be observed when larger loss and smaller gain bandwidths are considered. This points to gain narrowing mechanisms as a potential culprit for the discrepancy between the used HME model and the experiment.

In all cases, varying the gain bandwidth and loss to produce roughly 5 ps pulses results in significant chirp, suggesting the model is not fully capturing all the dynamics in the experiment. Another process easily introduced to the model is self-phase modulation (SPM). SPM is known to significantly disperse high-intensity pulses. In our model of SPM, we split the round-trip equation from the HME into two sections: the first simulates the pulse evolution in the gain chip while the second accounts for the round-trip propagation in the lithium niobate device. The SPM term is only included in the gain chip segment, as the coupling loss between the gain chip and LN results in reduced peak power in the LN section, such that we observe the SPM effect in LN to be comparatively negligible for reasonable values of n_2. The gain chip portion is additionally split into 10 steps; this enables the SPM to be more accurately modeled given the rapidly increasing pulse amplitude in the gain chip from the high gain. With reasonable estimates for gain saturation and gain chip mode size, the effect of varying n_2 is shown for both the β_- and β_+ solutions in Fig. S8a and S8b, respectively. It is worth noting that relatively large values of n_2 on the order of 10^{-18} m^2/W have been used. Here, we find that positive SPM results in strong pulse compression but quickly becomes unstable for both the β_- and β_+ solutions while negative SPM causes the broadening for the β_- solution and pulse shortening for the β_+ solution, with the β_- solution becoming unstable before the β_+ solution. Here, we again observe strong chirp for the broadened pulses, suggesting a discrepancy between the HME prediction and our experimental results.

In general, the inconsistencies between the HME results and our observed experimental results can be attributed to an admixture of difficulties in precisely quantifying certain system parameters, such as the nonlinear index of the gain chip, and the limitations of the HME itself. For example, the HME model treats the roundtrip as a single element, which ignores system dynamics occurring on faster timescales. Our breaking the round-trip propagation into segments for more accurate modeling of the SPM in the gain chip is an example of how one must be careful when making such a simplification in a system such as ours with such high gain and high loss. In addition, there may exist other effects in the semiconductor gain medium that are not captured by this simple model, such as the complex carrier dynamics and two-stage gain recovery in the III-V gain medium [8, 37], and spectrally selective cavity loss from intra-cavity etalon[22] or hole burning effects[38].

As such, the HME is useful in providing intuition behind the qualitative behavior of our device, such as the power scaling law shown in the main text Fig. 4F, and how the interplay between cavity dispersion and phase modulation leads to the pulse formation in our device. Meanwhile, its quantitative predictions should be viewed with the understanding that uncertainties in the measured system parameters exist, and the simplistic model does not account for all relevant phenomena that affect pulse formation. Further improvements to the model are needed to better capture the underlying physics of the experiment to more accurately predict the pulse characteristics of this device.

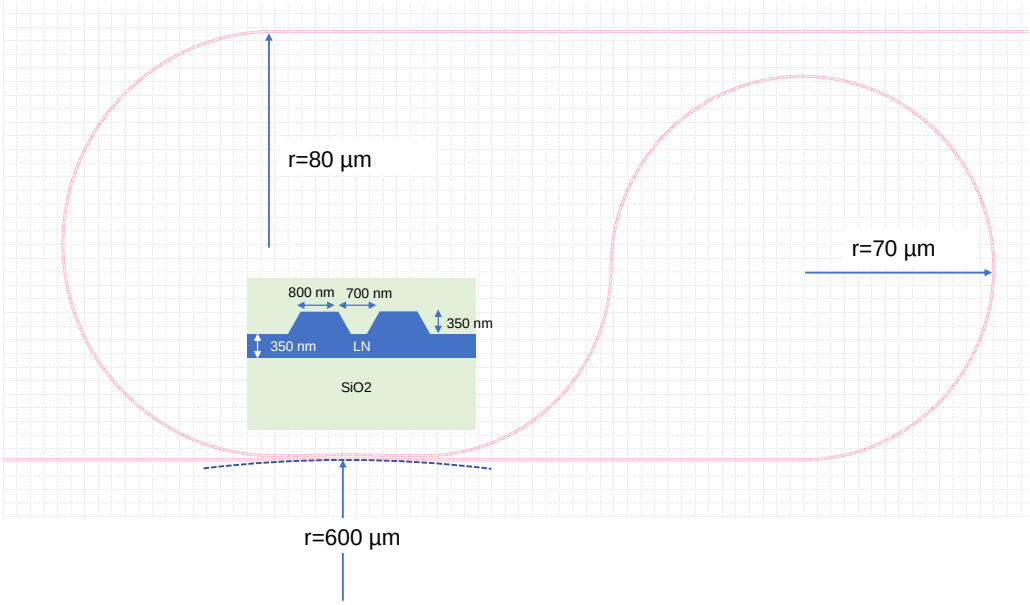

FIG. S1. Design of the broadband loop mirror with curved directional coupler. The inset shows the cross-section of the CDC region.

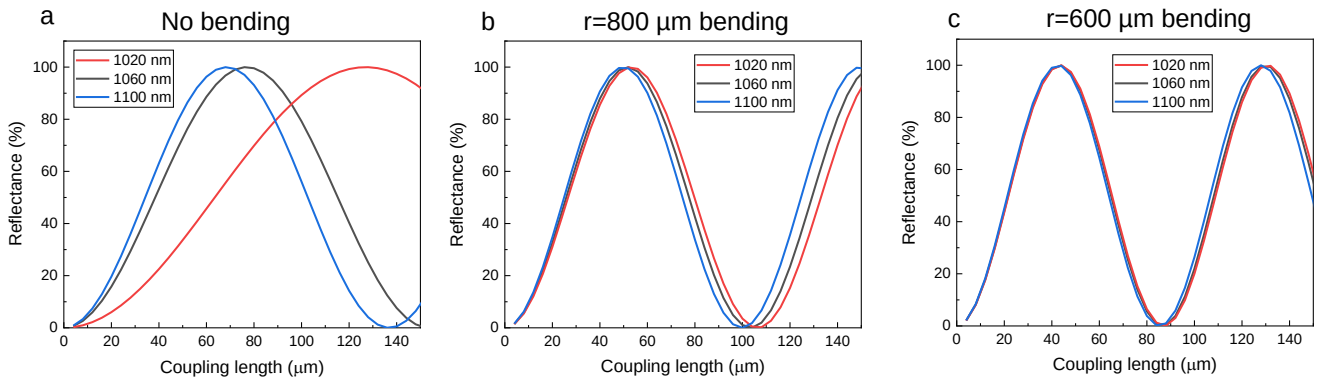

FIG. S2. Dependence of loop mirror reflectance on coupling length for (a) straight directional coupler, (b) curved directional coupler with 800 μm bending radius, and (c) curved directional coupler with 600 μm bending radius.

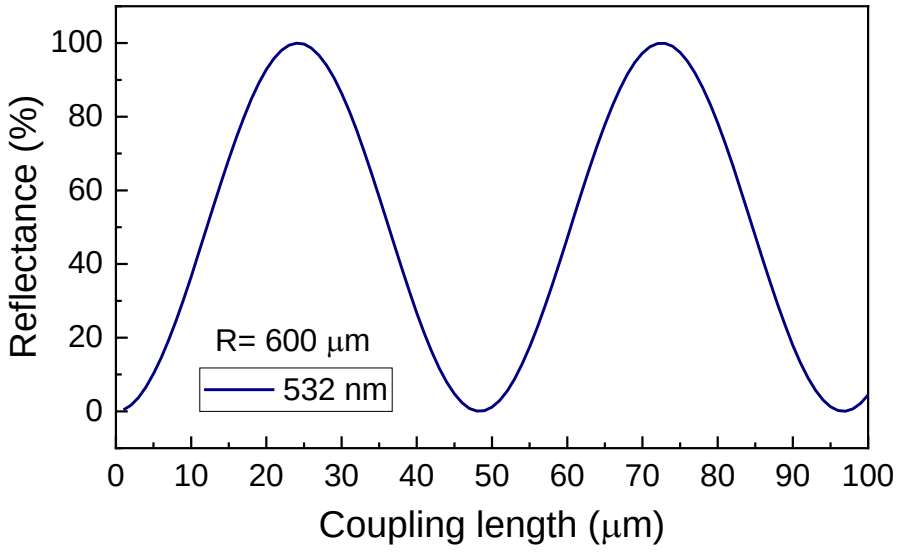

FIG. S3. Simulated loop mirror reflection as a function of coupling length at 532 nm. The loop mirror has a curved directional coupler with a bending radius (R) of 600 μm.

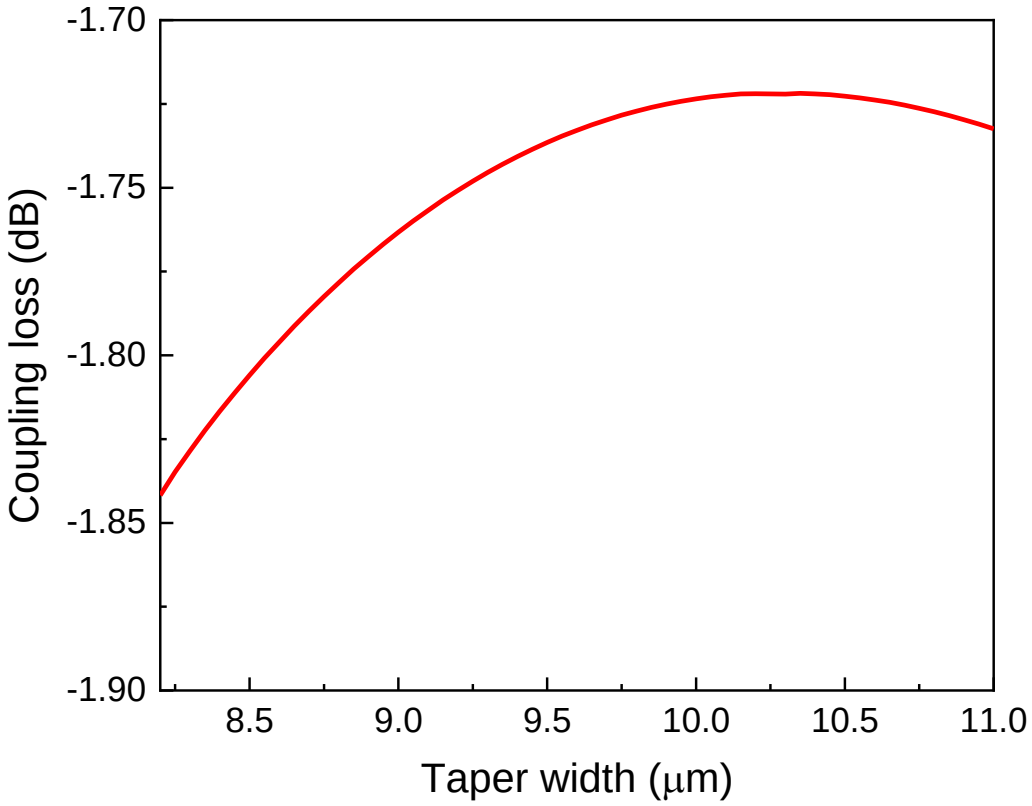

FIG. S4. Chip coupling loss as a function of taper width of LN nanophotonic waveguide.

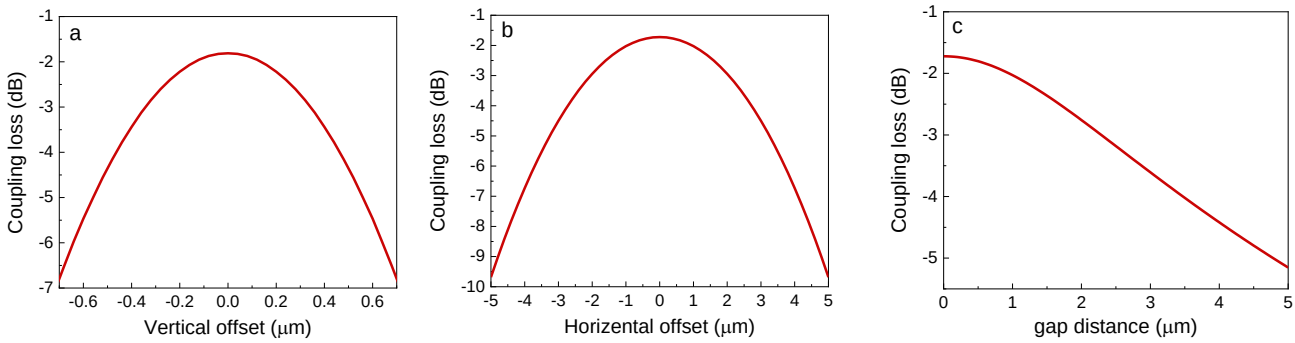

FIG. S5. (a) Dependence of coupling loss on the vertical offset. (b) Dependence of coupling loss on the horizontal offset. (c) Dependence of coupling loss on the gap distance between the gain chip and the TFLN chip.

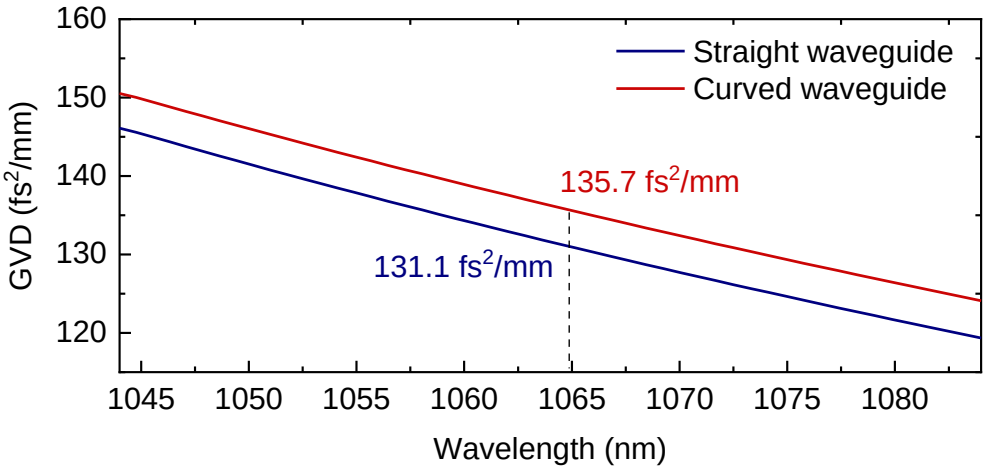

FIG. S6. Dependence of loop mirror reflectance on coupling length for (a) straight directional coupler, (b) curved directional coupler with 800 μm bending radius, and (c) curved directional coupler with 600 μm bending radius.

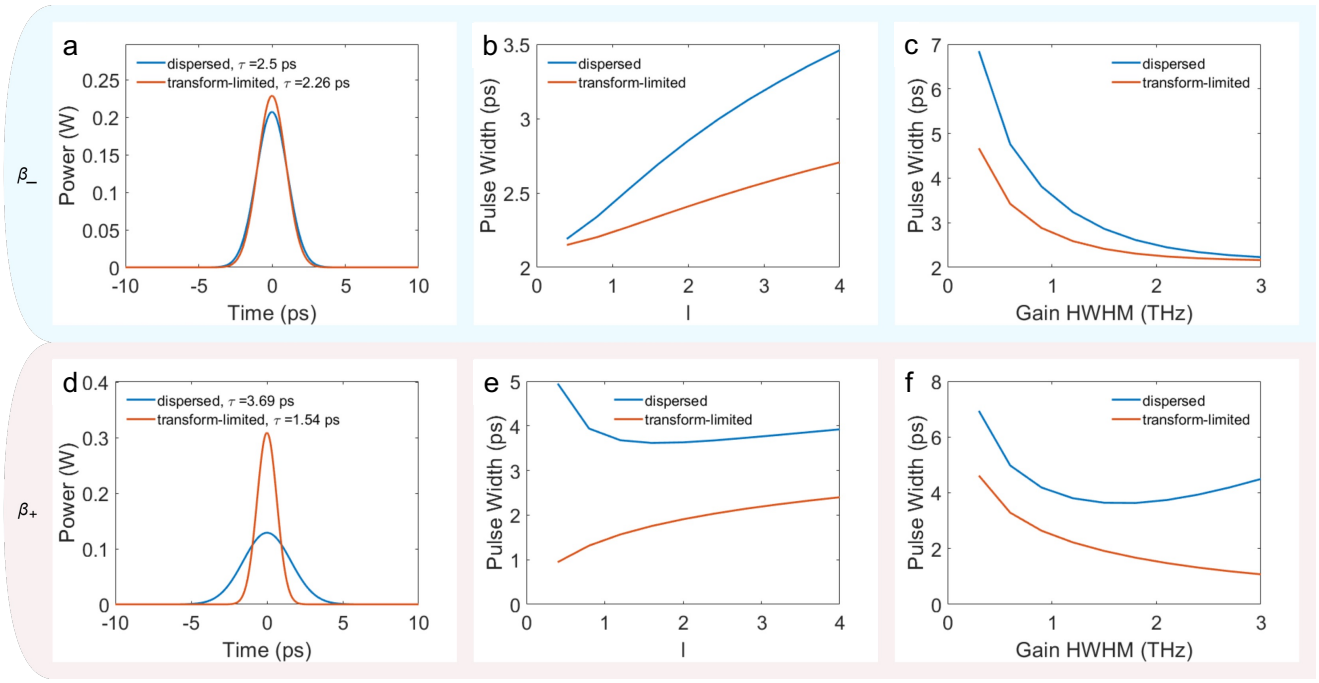

FIG. S7. Results from split-step Fourier simulations of the HME with GDD. In the top row, the β_- solution is shown where the phase modulator compensates for the cavity GDD. The bottom row shows the β_+ case, where the phase modulator adds to the chirp of the cavity GDD. The profile of the chirped and transform-limited pulses where $g = 1.15$ and the FWHM gain bandwidth is 4 THz are shown for the (a) β_- and (d) β_+ solutions. The pulse width as a function of loss (l) or gain with the gain bandwidth held constant at 4 THz is given for the (b) β_- and (e) β_+ solutions. Finally, the pulse width as a function of gain bandwidth with the loss held constant at 1.15 is shown for the (c) β_- and (f) β_+ solutions.

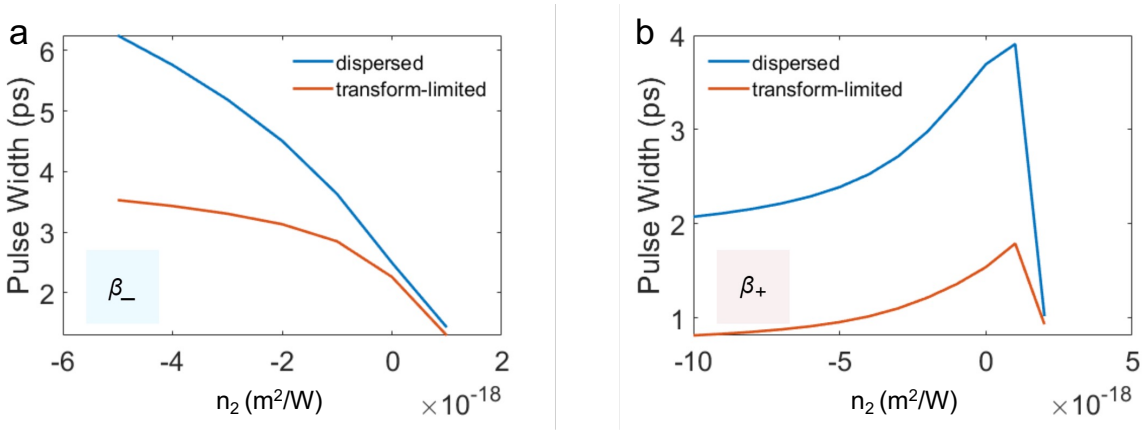

FIG. S8. Results from split-step Fourier simulations of the Haus master equation with GDD and SPM showing the FWHM pulse width as a function of n_2 for the (a) β_- and (b) β_+ solutions.

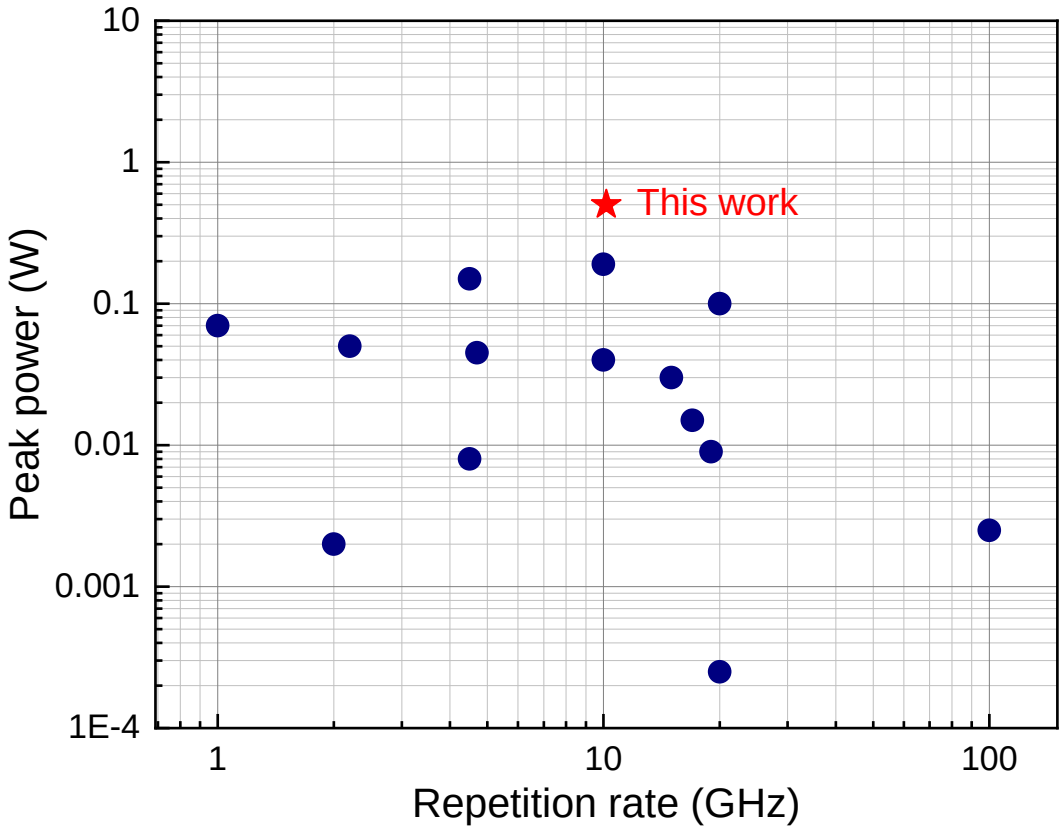

FIG. S9. Peak power comparison of nanophotonic waveguide integrated mode-locked lasers. Blue symbols are data points taken from from Ref. [7]

TABLE S1. Pulse characteristics of steady-state solutions of HME with GDD. The pulse width, chirp parameter (β), time-bandwidth product ($\Delta\tau\Delta\nu$), and transform-limited pulse width τ_{tl} are listed for each solution.

Parameter	β_-	β_+
τ_{p} [ps]	2.51	3.65
β	-0.471	2.122
$\Delta\tau\Delta\nu$	0.488	1.035
τ_{tl} [ps]	2.27	1.56

TABLE S2. Performance comparison of nanophotonic waveguide-integrated mode-locked lasers

Material platform	λ_c (nm)	f_{rep} (GHz)	Pulse width (ps)	On chip peak power (mW)	Footprint (mm^2)
III-V QW/TFLN (this work)	1065	10.17	4.81-5.03	500	1.5×4
III-V QW/SiN [31]	1610	3	8	250	9.5×0.6
III-V QW/SiN [9]	1567	2.18/15.5	3.1	8.32	N/A
III-V QW/SiN [10]	1064	4.06/6.09	6.032	80	N/A
III-V QW/Si [45]	1588.5	30	7	8.57	N/A
III-V QW/Si [46]	1604.5	40	4	16	N/A
III-V QW/Si [7]	1573	20	0.9	98	N/A
III-V QW/Si [47]	1600	1	7	50	N/A
III-V QD/GaAs [48]	1293	20	5.3	56	N/A

References and Notes

1. M. Wegener, *Extreme Nonlinear Optics: An Introduction* (Springer Science & Business Media, 2005).

2. J. M. Dudley, G. Genty, S. Coen, Supercontinuum generation in photonic crystal fiber. *Rev. Mod. Phys.* **78**, 1135–1184 (2006). doi:10.1103/RevModPhys.78.1135

3. A. D. Ludlow, M. M. Boyd, J. Ye, E. Peik, P. O. Schmidt, Optical atomic clocks. *Rev. Mod. Phys.* **87**, 637–701 (2015). doi:10.1103/RevModPhys.87.637

4. T. Udem, R. Holzwarth, T. W. Hänsch, Optical frequency metrology. *Nature* **416**, 233–237 (2002). doi:10.1038/416233a Medline

5. D. W. Piston, Imaging living cells and tissues by two-photon excitation microscopy. *Trends Cell Biol.* **9**, 66–69 (1999). doi:10.1016/S0962-8924(98)01432-9 Medline

6. A. Marandi, Z. Wang, K. Takata, R. L. Byer, Y. Yamamoto, Network of time-multiplexed optical parametric oscillators as a coherent Ising machine. *Nat. Photonics* **8**, 937–942 (2014). doi:10.1038/nphoton.2014.249

7. M. L. Davenport, S. Liu, J. E. Bowers, Integrated heterogeneous silicon/III–V mode-locked lasers. *Photon. Res.* **6**, 468 (2018). doi:10.1364/PRJ.6.000468

8. P. J. Delfyett, L. T. Florez, N. Stoffel, T. Gmitter, N. C. Andreadakis, Y. Silberberg, J. P. Heritage, G. A. Alphonse, High-power ultrafast laser diodes. *IEEE J. Quantum Electron.* **28**, 2203–2219 (1992). doi:10.1109/3.159528

9. A. Hermans, K. Van Gasse, J. Ø. Kjellman, C. Caër, T. Nakamura, Y. Inada, K. Hisada, T. Hirasawa, S. Cuyvers, S. Kumari, A. Marinins, R. Jansen, G. Roelkens, P. Soussan, X. Rottenberg, B. Kuyken, High-pulse-energy III-V-on-silicon-nitride mode-locked laser. *APL Photonics* **6**, 096102 (2021). doi:10.1063/5.0058022

10. E. Vissers, S. Poelman, H. Wenzel, H. Christopher, K. Van Gasse, A. Knigge, B. Kuyken, Hybrid integrated mode-locked laser using a GaAs-based 1064 nm gain chip and a SiN external cavity. *Opt. Express* **30**, 42394–42405 (2022). doi:10.1364/OE.474671 Medline

11. C. Wang, M. Zhang, X. Chen, M. Bertrand, A. Shams-Ansari, S. Chandrasekhar, P. Winzer, M. Lončar, Integrated lithium niobate electro-optic modulators operating at CMOS-compatible voltages. *Nature* **562**, 101–104 (2018). doi:10.1038/s41586-018-0551-y Medline

12. M. Xu, Y. Zhu, F. Pittalà, J. Tang, M. He, W. C. Ng, J. Wang, Z. Ruan, X. Tang, M. Kuschnerov, L. Liu, S. Yu, B. Zheng, X. Cai, Dual-polarization thin-film lithium niobate in-phase quadrature modulators for terabit-per-second transmission. *Optica* **9**, 61 (2022). doi:10.1364/OPTICA.449691

13. C. Wang, C. Langrock, A. Marandi, M. Jankowski, M. Zhang, B. Desiatov, M. M. Fejer, M. Lončar, Ultrahigh-efficiency wavelength conversion in nanophotonic periodically poled lithium niobate waveguides. *Optica* **5**, 1438 (2018). doi:10.1364/OPTICA.5.001438

14. J. Lu, J. B. Surya, X. Liu, A. W. Bruch, Z. Gong, Y. Xu, H. X. Tang, Periodically poled thin-film lithium niobate microring resonators with a second-harmonic generation efficiency of 250,000%/W. *Optica* **6**, 1455 (2019). doi:10.1364/OPTICA.6.001455

15. M. Jankowski, C. Langrock, B. Desiatov, A. Marandi, C. Wang, M. Zhang, C. R. Phillips, M. Lončar, M. M. Fejer, Ultrabroadband nonlinear optics in nanophotonic periodically poled lithium niobate waveguides. *Optica* **7**, 40 (2020). doi:10.1364/OPTICA.7.000040

16. L. Ledezma, A. Roy, L. Costa, R. Sekine, R. Gray, Q. Guo, R. Nehra, R. M. Briggs, A. Marandi, Octave-spanning tunable infrared parametric oscillators in nanophotonics. *Sci. Adv.* **9**, eadf9711 (2023). doi:10.1126/sciadv.adf9711 Medline

17. J. Lu, A. Al Sayem, Z. Gong, J. B. Surya, C.-L. Zou, H. X. Tang, Ultralow-threshold thin-film lithium niobate optical parametric oscillator. *Optica* **8**, 539 (2021). doi:10.1364/OPTICA.418984

18. T. P. McKenna, H. S. Stokowski, V. Ansari, J. Mishra, M. Jankowski, C. J. Sarabalis, J. F. Herrmann, C. Langrock, M. M. Fejer, A. H. Safavi-Naeini, Ultra-low-power second-order nonlinear optics on a chip. *Nat. Commun.* **13**, 4532 (2022). doi:10.1038/s41467-022-31134-5 Medline

19. A. Roy, R. Nehra, S. Jahani, L. Ledezma, C. Langrock, M. Fejer, A. Marandi, Temporal walk-off induced dissipative quadratic solitons. *Nat. Photonics* **16**, 162–168 (2022). doi:10.1038/s41566-021-00942-4

20. Q. Guo, R. Sekine, L. Ledezma, R. Nehra, D. J. Dean, A. Roy, R. M. Gray, S. Jahani, A. Marandi, Femtojoule femtosecond all-optical switching in lithium niobate nanophotonics. *Nat. Photonics* **16**, 625–631 (2022). doi:10.1038/s41566-022-01044-5

21. R. Nehra, R. Sekine, L. Ledezma, Q. Guo, R. M. Gray, A. Roy, A. Marandi, Few-cycle vacuum squeezing in nanophotonics. *Science* **377**, 1333–1337 (2022). doi:10.1126/science.abo6213 Medline

22. D. Kuizenga, A. Siegman, FM and AM mode locking of the homogeneous laser - Part I: Theory. *IEEE J. Quantum Electron.* **6**, 694–708 (1970). doi:10.1109/JQE.1970.1076343

23. R. Nagar, D. Abraham, G. Eisenstein, Pure phase-modulation mode locking in semiconductor lasers. *Opt. Lett.* **17**, 1119–1121 (1992). doi:10.1364/OL.17.001119 Medline

24. M. Zhang, B. Buscaino, C. Wang, A. Shams-Ansari, C. Reimer, R. Zhu, J. M. Kahn, M. Lončar, Broadband electro-optic frequency comb generation in a lithium niobate microring resonator. *Nature* **568**, 373–377 (2019). doi:10.1038/s41586-019-1008-7 Medline

25. M. Yu, D. Barton Iii, R. Cheng, C. Reimer, P. Kharel, L. He, L. Shao, D. Zhu, Y. Hu, H. R. Grant, L. Johansson, Y. Okawachi, A. L. Gaeta, M. Zhang, M. Lončar, Integrated femtosecond pulse generator on thin-film lithium niobate. *Nature* **612**, 252–258 (2022). doi:10.1038/s41586-022-05345-1 Medline

26. Y. Hu, M. Yu, B. Buscaino, N. Sinclair, D. Zhu, R. Cheng, A. Shams-Ansari, L. Shao, M. Zhang, J. M. Kahn, M. Lončar, High-efficiency and broadband on-chip electro-optic frequency comb generators. *Nat. Photonics* **16**, 679–685 (2022). doi:10.1038/s41566-022-01059-y

27. A. Rueda, F. Sedlmeir, M. Kumari, G. Leuchs, H. G. L. Schwefel, Resonant electro-optic frequency comb. *Nature* **568**, 378–381 (2019). doi:10.1038/s41586-019-1110-x Medline

28. J. P. Salvestrini, L. Guilbert, M. Fontana, M. Abarkan, S. Gille, Analysis and Control of the DC Drift in LiNbO 3 Based Mach–Zehnder Modulators. *J. Lightwave Technol.* **29**, 1522–1534 (2011). doi:10.1109/JLT.2011.2136322

29. M. Jin, J. Chen, Y. Sua, P. Kumar, Y. Huang, Efficient electro-optical modulation on thin-film lithium niobate. *Opt. Lett.* **46**, 1884–1887 (2021). doi:10.1364/OL.419597 Medline

30. C. Hu, A. Pan, T. Li, X. Wang, Y. Liu, S. Tao, C. Zeng, J. Xia, High-efficient coupler for thin-film lithium niobate waveguide devices. *Opt. Express* **29**, 5397–5406 (2021). doi:10.1364/OE.416492 Medline

31. E. Vissers, S. Poelman, C. O. de Beeck, K. Van Gasse, B. Kuyken, Hybrid integrated mode-locked laser diodes with a silicon nitride extended cavity. *Opt. Express* **29**, 15013–15022 (2021). doi:10.1364/OE.422621 Medline

32. F. Kärtner, D. Zumbühl, N. Matuschek, Turbulence in Mode-Locked Lasers. *Phys. Rev. Lett.* **82**, 4428–4431 (1999). doi:10.1103/PhysRevLett.82.4428

33. U. Keller, R. Paschotta, *Ultrafast Lasers* (Springer, 2021).

34. A. E. Siegman, *Lasers* (University Science Books, 1986).

35. H. A. Haus, Mode-locking of lasers. *IEEE J. Sel. Top. Quantum Electron.* **6**, 1173–1185 (2000). doi:10.1109/2944.902165

36. Q. Guo, data and computer code for "Ultrafast mode-locked laser in nanophotonic lithium niobate", version 2, Figshare (2023); https://doi.org/10.6084/m9.figshare.24208434.

37. G. P. Agrawal, N. A. Olsson, Self-phase modulation and spectral broadening of optical pulses in semiconductor laser amplifiers. *IEEE J. Quantum Electron.* **25**, 2297–2306 (1989). doi:10.1109/3.42059

38. A. Uskov, J. Mork, J. Mark, Wave mixing in semiconductor laser amplifiers due to carrier hating and spectral-hole burning. *IEEE J. Quantum Electron.* **30**, 1769–1781 (1994). doi:10.1109/3.301641

39. S. Schmitt-Rink, D. S. Chemla, D. A. Miller, Theory of transient excitonic optical nonlinearities in semiconductor quantum-well structures. *Phys. Rev. B Condens. Matter* **32**, 6601–6609 (1985). doi:10.1103/PhysRevB.32.6601 Medline

40. D. E. Zelmon, D. L. Small, D. Jundt, Infrared corrected Sellmeier coefficients for congruently grown lithium niobate and 5 mol% magnesium oxide –doped lithium niobate. *J. Opt. Soc. Am. B* **14**, 3319 (1997). doi:10.1364/JOSAB.14.003319

41. T. Mitarai, E. Moataz, T. Miyazaki, T. Amemiya, N. Nishiyama, Design and measurement of broadband loop mirror with curved directional coupler based on Si waveguides. *Jpn. J. Appl. Phys.* **59**, 112002 (2020). doi:10.35848/1347-4065/abbe68

42. H. Morino, T. Maruyama, K. Iiyama, Reduction of Wavelength Dependence of Coupling Characteristics Using Si Optical Waveguide Curved Directional Coupler. *J. Lightwave Technol.* **32**, 2188–2192 (2014). doi:10.1109/JLT.2014.2321660

43. A. Yariv, P. Yeh, *Photonics: Optical Electronics in Modern Communications* (Oxford Univ. Press, 2007).

44. W. K. Burns, A. F. Milton, A. B. Lee, Optical waveguide parabolic coupling horns. *Appl. Phys. Lett.* **30**, 28–30 (1977). doi:10.1063/1.89199

45. A. W. Fang, B. R. Koch, K.-G. Gan, H. Park, R. Jones, O. Cohen, M. J. Paniccia, D. J. Blumenthal, J. E. Bowers, A racetrack mode-locked silicon evanescent laser. *Opt. Express* **16**, 1393–1398 (2008). doi:10.1364/OE.16.001393 Medline

46. B. R. Koch, A. W. Fang, O. Cohen, J. E. Bowers, Mode-locked silicon evanescent lasers. *Opt. Express* **15**, 11225–11233 (2007). doi:10.1364/OE.15.011225 Medline

47. Z. Wang, K. Van Gasse, V. Moskalenko, S. Latkowski, E. Bente, B. Kuyken, G. Roelkens, A III-V-on-Si ultra-dense comb laser. *Light Sci. Appl.* **6**, e16260 (2017). doi:10.1038/lsa.2016.260 Medline

48. Z. Zhang, J. C. Norman, S. Liu, A. Malik, J. E. Bowers, Integrated dispersion compensated mode-locked quantum dot laser. *Photon. Res.* **8**, 1428 (2020). doi:10.1364/PRJ.397175